Modelling Hybrid Acoustofluidic Devices for Enhancing Nano- and Micro-Particle Manipulation in Microfluidics

Hanlin Wang[1], Fan Yuan[2], Zhihua Xie[3], Chao Sun[4], Fangda Wu[1], Roman Mikhaylov[1], Minghong Shen[5], Jian Yang[5], You Zhou[6], Dongfang Liang[7], Xianfang Sun[8], Zhenlin Wu[9], Zhiyong Yang[10], Xin Yang[1]

[1] Department of Electrical and Electronic Engineering, School of Engineering, Cardiff University, UK CF24 3AA

[2] Department of Biomedical Engineering, School of Engineering, Duke University, NC 27708-0281, USA

[3] Department of Civil Engineering, School of Engineering, Cardiff University, UK CF24 3AA

[4] School of Life Sciences, Northwestern Polytechnical University, 710072, P.R. China

[5] Division of Cancer and Genetics, School of Medicine, Cardiff University, UK CF14 4XN

[6] Systems Immunity Research Institute, School of Medicine, Cardiff University, UK CF14 4XN

[7] Department of Engineering, University of Cambridge, UK CB2 1PZ

[8] School of Computer Science, Cardiff University, UK CF24 3AA

[9] School of Optoelectronic Engineering and Instrumentation Science, Dalian University of Technology, 116023, P.R. China

[10] School of Mechanical Engineering, Tianjin University, 300072, P.R. China

Abstract

Acoustofluidic techniques are increasingly used to manipulate nano- and micro-particles in microfluidics. A wide range of acoustofluidic devices consisting of microchannels and acoustic sources have been developed for applications in biochemistry and biomedicine. In this work, two hybrid acoustofluidic devices are developed and modelled, including a double surface acoustic wave (SAW) transducer and a PZT-SAW transducer. The numerical study to these devices demonstrates a higher acoustic pressure present in the microchannel resulting in larger particle velocities in migration to the pressure nodes. The amplitude of the acoustic pressure and the pattern of the pressure distribution can be controlled in the hybrid transducers. By sweeping the height and width of the microchannel, one can identify an optimum dimension to produce intensive acoustic pressure in the PZT-SAW transducer. The particle trajectories reveal that both the SAW-SAW and PZT-SAW configurations produce significantly higher acoustic pressure and particle velocity in the microchannel. This work provides new insights to design acoustofluidic devices with more than one SAW transducer to effectively manipulate micro- and nano-particles.

Key words: acoustofluidics, numerical simulations, microparticles manipulations, microchannel

1. Introduction

Recently, acoustofluidic manipulation of micro- and nano-particles, such as bacteria [1-3], blood cells [4-9], circulating tumour cells (CTCs) [10-12], and extracellular vesicles [13-15] has attracted significant attention. Acoustofluidic devices are applied in biochemical, biophysical, and biomedical areas due to their biocompatible, versatile, contactless, and label-free advantages [16, 17].

Acoustofluidic devices using bulk acoustic waves (BAWs) are set up in the entire device and used in systems with acoustically hard structures, in which the acoustic energy is coupled to the water in the microchannel through these hard materials such as silicone and Pyrex. The BAW resonance relies on the high acoustic impedance ratio between the wall and the water at the water-wall interface [18-20]. Piezoelectric transducer (PZT) is commonly used to produce acoustic waves in BAW devices. Devices based on surface acoustic waves (SAWs) can induce acoustophoretic motion independent of the acoustic impedance ratio at the boundary, which allows the microchannel to be made by either acoustically hard or soft materials, e.g., polydimethylsiloxane (PDMS). The versatility of SAW devices also enables droplet manipulation with free boundary conditions [21-25]. Interdigital electrodes patterned on piezoelectric substrates such as lithium niobate ($LiNbO_3$) to form interdigital transducers (IDTs) are commonly used to produce Rayleigh waves in SAW devices.

The acoustic radiation force rising from the scattering of the acoustic waves on the particles and the Stokes drag force from induced acoustic streaming are the main factors determining the trajectory of the particles in the acoustofluidic device. Any particle larger than the transition size is dominantly driven by the radiation force[26], while particles smaller than the transition size are mainly affected by the Stokes drag force. Due to the difficulty in measuring the two forces experimentally, numerical models have been used extensively to simulate the particle movement or verify the experimental findings [27-30]. In applications of acoustofluidics for high-throughput particle separations, a pseudo-standing wave (PSW) was shown to travel towards the upper wall of the microchannel, which causes vertical oscillation of the pressure field in the microchannel to produce another standing wave [31]. The PSW could be strengthened by topping a glass slide as the reflector in the microchannel [32, 33]. In the current study, we propose to replace the glass reflector with an active acoustic source on the top of the microchannel. The active source could then act as an adjustable actuator, and further enhance the acoustic pressure for manipulating particles in the microchannel.

To investigate the effectiveness of the hybrid SAW devices, we developed numerical models to study the acoustic pressure and the trajectory of microparticles in the device. Factors such as boundary vibration, channel materials, and dimensions are taken into account. The simulation results of two types of hybrid acoustofluidic structures are compared with the conventional devices. The importance of the hybrid acoustofluidic device is to offer a more effective tool to manipulate bioparticles with the potential to reduce the device footprint.

2. Methods

When acoustic wave is applied to a suspension of nano- or micro-particles, it will exert acoustic radiation force on the particles, due to the scattering of the wave, which has been utilised to manipulate the particles. To achieve desired distribution patterns of the particles in a microchannel of acoustofluidic devices, we performed numerical simulations for different design scenarios. In all cases, the microchannel length is significantly longer than the height and the width, and the acoustic waves are perpendicular to the longitudinal direction. Thus, the fluid flow and particle movement in the microchannel are investigated as two-dimensional problems.

A. Governing equations for fluid flow

For very dilute suspensions, particle influences on the bulk fluid flow can be neglected as long as the particle size is significantly smaller than the microchannel dimensions and the acoustic wavelength. The governing equations for the bulk fluid flow are [30],

$$\frac{\partial \hat{\rho}}{\partial t} = -\boldsymbol{\nabla} \cdot (\hat{\rho}\hat{\boldsymbol{v}}) \tag{1}$$

$$\hat{\rho}\frac{\partial \hat{\boldsymbol{v}}}{\partial t} = -\boldsymbol{\nabla}\hat{p} - \hat{\rho}(\hat{\boldsymbol{v}} \cdot \boldsymbol{\nabla})\hat{\boldsymbol{v}} + \eta\boldsymbol{\nabla}^2\hat{\boldsymbol{v}} + \beta\eta\boldsymbol{\nabla}(\boldsymbol{\nabla} \cdot \hat{\boldsymbol{v}}) \tag{2}$$

where

$$\beta = \frac{\eta_\mathrm{b}}{\eta} + \frac{1}{3}, \tag{3}$$

$\hat{\rho}$ is the fluid density, the bold letter $\hat{\boldsymbol{v}}$ is the vector of fluid velocity, $\hat{p}$ is the fluid pressure, η and η_b are the shear and bulk viscosities, respectively.

Prior to the application of acoustic waves, there is no fluid flow in the acoustofluidic devices. Thus, the fluid mass density and pressure, ρ_0 and p_0, are uniform and time-independent. The application of acoustic waves to the fluid causes small perturbations in the mass density, fluid pressure, and velocity fields, which can be expressed as,

$$\hat{p} = p_0 + \hat{p}_1 + \hat{p}_2 + \cdots \tag{4}$$

$$\hat{\rho} = \rho_0 + \hat{\rho}_1 + \hat{\rho}_2 + \cdots \tag{5}$$

$$\hat{\boldsymbol{v}} = \hat{\boldsymbol{v}}_\mathbf{1} + \hat{\boldsymbol{v}}_\mathbf{2} + \cdots \tag{6}$$

where the subscripts 1 and 2 indicate the first and the second order terms, respectively. Higher order terms are neglected in the simulations. The first order pressure $\hat{p}_1$ is assumed to be proportional to $\hat{\rho}_1$[34],

$$\hat{p}_1 = c_0^2 \hat{\rho}_1 \tag{7}$$

where c_0 is the proportionality constant that is approximately equal to the speed of sound in the fluid. Substituting Eq. (4) through (7) into Eqs. (1) and (2) yields the continuity and momentum equations for the first- and second-order terms:

$$\frac{1}{c_0^2}\frac{\partial \hat{p}_1}{\partial t} = -\rho_0 \boldsymbol{\nabla} \cdot \hat{\boldsymbol{v}}_\mathbf{1} \tag{8}$$

$$\rho_0 \frac{\partial \hat{\boldsymbol{v}}_\mathbf{1}}{\partial t} = -\boldsymbol{\nabla}\hat{p}_1 + \eta \boldsymbol{\nabla}^2 \hat{\boldsymbol{v}}_\mathbf{1} + \beta\eta\boldsymbol{\nabla}(\boldsymbol{\nabla}\cdot\hat{\boldsymbol{v}}_\mathbf{1}) \tag{9}$$

$$\frac{\partial \hat{\rho}_2}{\partial t} = -\rho_0 \boldsymbol{\nabla}\cdot\hat{\boldsymbol{v}}_\mathbf{2} - \boldsymbol{\nabla}\cdot(\hat{\rho}_1\hat{\boldsymbol{v}}_\mathbf{1}) \tag{10}$$

$$\rho_0 \frac{\partial \hat{\boldsymbol{v}}_\mathbf{2}}{\partial t} = -\boldsymbol{\nabla}\hat{p}_2 + \eta \boldsymbol{\nabla}^2 \hat{\boldsymbol{v}}_\mathbf{2} + \beta\eta\boldsymbol{\nabla}(\boldsymbol{\nabla}\cdot\hat{\boldsymbol{v}}_\mathbf{2}) - \hat{\rho}_1\frac{\partial \hat{\boldsymbol{v}}_\mathbf{1}}{\partial t} - \rho_0(\hat{\boldsymbol{v}}_\mathbf{1}\cdot\boldsymbol{\nabla})\hat{\boldsymbol{v}}_\mathbf{1} \tag{11}$$

If the acoustic perturbation is temporally periodic, averaging Eqs. (10) and (11) over a period yields

$$\rho_0\boldsymbol{\nabla}\cdot\langle\hat{\boldsymbol{v}}_\mathbf{2}\rangle = -\boldsymbol{\nabla}\cdot\langle\hat{\rho}_1\hat{\boldsymbol{v}}_\mathbf{1}\rangle \tag{12}$$

$$-\nabla\langle\hat{p}_2\rangle + \eta\nabla^2\langle\hat{\boldsymbol{v}}_{\mathbf{2}}\rangle + \beta\eta\nabla(\nabla\cdot\langle\hat{\boldsymbol{v}}_{\mathbf{2}}\rangle) = \langle\hat{\rho}_1\frac{\partial\hat{\boldsymbol{v}}_{\mathbf{1}}}{\partial t}\rangle + \rho_0\langle(\hat{\boldsymbol{v}}_{\mathbf{1}}\cdot\nabla)\hat{\boldsymbol{v}}_1\rangle \tag{13}$$

where $\langle X\rangle$ denotes the average of X over the period. In the study, we further assumed the first-order density, pressure, and velocity to be harmonic time dependence, i.e.

$$\hat{\rho}_1(\boldsymbol{r},t) = Re\left[\rho_1 e^{\mathrm{i}\omega t}\right] \tag{14}$$

$$\hat{p}_1(\boldsymbol{r},t) = Re\left[p_1 e^{\mathrm{i}\omega t}\right] \tag{15}$$

$$\hat{\boldsymbol{v}}_1(\boldsymbol{r},t) = Re\left[\boldsymbol{v}_1 e^{\mathrm{i}\omega t}\right] \tag{16}$$

where ω is the angular frequency, ρ_1, p_1, and $\boldsymbol{v}_1$ are time dependent but may vary with the spatial location and ω. It is equal to the wave frequency f multiplied by 2π. From Eq. (7), it can be shown mathematically that $p_1 = c_0^2\rho_1$. Substituting the complex mass density, pressure, and velocity in Eqs. (15) and (16) into Eqs. (8) and (9) yields the governing equations for solving p_1 and $\boldsymbol{v}_{\mathbf{1}}$,

$$\frac{\mathrm{i}\omega p_1}{c_0^2} = -\rho_0\nabla\cdot\boldsymbol{v}_{\mathbf{1}} \tag{17}$$

$$\mathrm{i}\omega\rho_0\boldsymbol{v}_{\mathbf{1}} = -\nabla p_1 + \eta\nabla^2\boldsymbol{v}_{\mathbf{1}} + \beta\eta\nabla(\nabla\cdot\boldsymbol{v}_{\mathbf{1}}) \tag{18}$$

Substituting the complex mass density, pressure, and velocity in Eqs. (14) through (16) into Eqs. (12) and (13) yields governing equations for solving $\langle\hat{\boldsymbol{v}}_{\mathbf{2}}\rangle$ and $\langle\hat{p}_2\rangle$,

$$\rho_0\nabla\cdot\langle\hat{\boldsymbol{v}}_{\mathbf{2}}\rangle = -\frac{1}{2}\mathrm{Re}[\nabla\cdot(\rho_1^*\boldsymbol{v}_1)] \tag{19}$$

$$\eta\nabla^2\langle\hat{\boldsymbol{v}}_{\mathbf{2}}\rangle - \nabla\langle\hat{p}_2\rangle = \frac{1}{2}\mathrm{Re}(\mathrm{i}\omega\rho_1^*\boldsymbol{v}_1) + \frac{\rho_0}{2}\mathrm{Re}(\boldsymbol{v}_1^*\cdot\nabla\boldsymbol{v}_1) + \frac{\eta\beta}{2\rho_0}\mathrm{Re}\{\nabla[\nabla\cdot(\rho_1^*\boldsymbol{v}_1)]\} \tag{20}$$

where the asterisk denotes the complex conjugate of the quantity.

B. Governing equation for acoustophoretic trajectories of particles

The acoustic wave causes the fluid flow and the asymmetric oscillation of the particles in the suspension. The net movement of a particle depends on the time-averaged acoustic radiation force $\boldsymbol{F}^{\mathrm{rad}}$ on the particle that can be calculated as the sum of the second-order pressure and the first-order momentum flux integrated over a fixed surface, $\partial\Omega$, in the bulk fluid around the particle,

$$\boldsymbol{F}^{\mathrm{rad}} = -\oiint_{\partial\Omega} \langle \boldsymbol{n} \cdot [\hat{p}_2 \boldsymbol{I} + \rho_0 (\hat{\boldsymbol{v}}_1 \hat{\boldsymbol{v}}_1)] \rangle \mathrm{d}A \tag{21}$$

where $\boldsymbol{n}$ is the unit normal vector of the particle surface directed into the fluid, $\boldsymbol{I}$ is the unit tensor. If the particle is spherical and its radius, a, is much smaller than the wavelength, an analytical expression of the force has been derived by Settnes and Bruus[36],

$$\boldsymbol{F}^{\mathrm{rad}} = -\pi a^3 \left[\frac{2\kappa_0}{3} \mathrm{Re}(f_1^* p_1^* \boldsymbol{\nabla} p_1) - \rho_0 \mathrm{Re}(f_2^* \boldsymbol{v}_1^* \boldsymbol{\nabla} \boldsymbol{v}_1) \right] \tag{22}$$

where f_1 and f_2 are the scattering coefficients, and κ_0 is the isentropic compressibility of the fluid defined as,

$$\kappa_0 = -\frac{1}{V} \left(\frac{\partial V}{\partial \hat{p}} \right)_S = \frac{1}{\hat{\rho}} \left(\frac{\partial \hat{\rho}}{\partial \hat{p}} \right)_S, \tag{23}$$

V and S are the volume and entropy of the fluid. By neglecting the second and the higher order terms, it can be shown that $\kappa_0 = 1/(\rho_0 c_0^2)$.[34] The scattering coefficients can be calculated by

$$f_1 = 1 - \frac{\kappa_{\mathrm{p}}}{\kappa_0} \tag{24}$$

$$f_2 = \frac{2(1-\gamma)(\rho_{\mathrm{p}} - \rho_0)}{2\rho_{\mathrm{p}} + \rho_0 (1 - 3\gamma)} \tag{25}$$

where

$$\gamma = -\frac{3}{2} \left[1 + \mathrm{i} \left(1 + \frac{\delta}{a} \right) \right] \frac{\delta}{a} \tag{26}$$

$$\delta = \sqrt{\frac{2\eta}{\omega \rho_0}} \tag{27}$$

ρ_p and κ_p are the mass density and the compressibility of the particle, respectively. δ is called the viscous penetration depth or the characteristic thickness of the viscous boundary layer [37]. Apart from $\boldsymbol{F}^\mathrm{rad}$, the particle also experiences a drag from the surrounding fluid. Since the time-averaged streaming velocity is $\langle \widehat{\boldsymbol{v}}_2 \rangle$, the time-averaged drag is,

$$\boldsymbol{F}^\mathrm{drag} = 6\pi\eta a\big(\langle \widehat{\boldsymbol{v}}_\mathbf{2} \rangle - \boldsymbol{v}_{\boldsymbol{p}}\big) \tag{28}$$

where $\boldsymbol{v}_\mathrm{p}$ is the particle velocity. Based on the Newton's second law of motion, the governing equation for the particle movement is,

$$\frac{d\big(m_p \boldsymbol{v}_p\big)}{dt} = \boldsymbol{F}^\mathrm{rad} + \boldsymbol{F}^\mathrm{drag} \tag{29}$$

where m_p is the particle mass. Eq. (29) was used to calculate the particle velocity and trajectory after p_1, $\boldsymbol{v}_1$, and $\langle \widehat{\boldsymbol{v}}_\mathbf{2} \rangle$ were obtained by numerically solving Eqs. (17) through (20) under the boundary conditions described below.

C. Model configurations and boundary conditions

C1. Model configurations

Four different model configurations were considered in the study. The typical SAW transducer made by patterning a pair of interdigital electrodes on an $LiNbO_3$ substrate bonded to a PDMS microchannel is shown in **Fig. 1(a)**. Operating under the same radio frequency (RF) signal, two SAWs generated by the IDTs counter-propagate on the substrate to produce a standing SAW (SSAW) within the microchannel. Stable acoustic pressure gradients are formed in the water flowing in the microchannel which exerts acoustic radiation force and streaming drag force on the particles inside the microchannel. This model configuration is called SAW-PDMS. **Fig. 1(b)** shows the model of a novel structure of an acoustofluidic chip for high throughput CTC separation [32, 33], which employs a glass slide as the acoustic reflector attached on the top of the microchannel, namely hybrid PDMS-glass resonator (we call it SAW-Glass). The reflector prevents the acoustic energy loss caused by the PDMS absorption on the top.

To further increase the acoustic pressure in the microchannel for enhanced manipulation of nano- and micro-particles, two new acoustofluidic structures have been developed, as shown in **Fig. 1(c)** and **Fig. 1(d)**. In **Fig. 1(c)**, the PDMS wall of the microchannel is sandwiched between two identical SAW transducers, we call this structure as SAW-SAW. The SAW-SAW model can provide stronger acoustic pressure gradients in the microchannel. By tuning the phase difference between the top and bottom SAW transducers, the acoustic pressure distribution can be controlled. The model shown in **Fig. 1(d)** is similar to that shown in **Fig. 1(c)**, except the top is replaced by a PZT. This structure is called PZT-SAW. The RF signals are driving both the PZT and SAW transducers to produce an integrated acoustic field in the microchannel. Changing the input parameters such as the frequency and voltage of the PZT and SAW transducers can vary the integrated acoustic field. **Fig. 1(e)** shows the computational domain of the model. The microchannel width (W) and the height (H) are 600 µm and 125 µm, respectively. Γ_t, Γ_b, and Γ_s denote the top, bottom, and side walls, respectively. Other parameter values used in the numerical simulations are shown in **Table 1**.

C2. Boundary conditions

The simulations were performed using a finite element method implemented in the COMSOL software (version 5.4). To solve Eqs. (17) and (18) for determining p_1 and $\boldsymbol{v}_1$, we employed the impedance or lossy-wall boundary condition at the water-PDMS and water-glass interfaces where the energy of the acoustic wave is partially absorbed by the solid walls [32,34]. After neglecting the higher order terms, the boundary condition at these interfaces is given by

$$\boldsymbol{n}\cdot\left[-p_1\boldsymbol{I}+\eta(\boldsymbol{\nabla v_1}+(\boldsymbol{\nabla v_1})^T)-\left(\frac{2}{3}\eta-\eta_b\right)(\boldsymbol{\nabla}\cdot\boldsymbol{v_1})\boldsymbol{I}\right]=-Z_0(\boldsymbol{n}\cdot\boldsymbol{v_1})\boldsymbol{n} \qquad (30)$$

where Z_0 is the acoustic impedance of the wall. Its values for different wall materials are shown in **Table 1**. To derive the boundary condition at the water-$LiNbO_3$ interface, we considered the $LiNbO_3$ substrate to be actuated by the SAW, and ignored the wave decay along the propagation path in the substrate because of the short path length. Specifically, we assumed the displacement of the substrate in the normal direction of a wall to be [38],

$$\hat{\boldsymbol{u}} = Re\left(u_0 \mathrm{i}\left(e^{\mathrm{i}[\omega t - k_\mathrm{s}(W/2+y)]} - e^{\mathrm{i}[\omega t - k_\mathrm{s}(W/2+y)]}\right)\right)\boldsymbol{n} \tag{31}$$

where u_0, t, k_s, and y denote the displacement amplitude, the time, the angular wave number, and the y coordinate, respectively. Taking partial derivative of $\hat{\boldsymbol{u}}$ with respect to time yields the substrate velocity,

$$\hat{\boldsymbol{v}} = Re\left(-\omega u_0 (e^{\mathrm{i}[\omega t - k_\mathrm{s}(W/2+y)]} - e^{\mathrm{i}[\omega t - k_\mathrm{s}(W/2+y)]}\right)\boldsymbol{n} \tag{32}$$

Neglecting the higher order terms, the continuity of the velocity at the water-$LiNbO_3$ interface requires,

$$\boldsymbol{v_1} = -\omega u_0\left[e^{-\mathrm{i}k_\mathrm{s}(W/2+y)} - e^{-\mathrm{i}k_\mathrm{s}(W/2-y)}\right]\boldsymbol{n} \tag{33}$$

For the SAW-SAW configuration, Eq. (32) is used as the velocity boundary condition on the bottom wall. For the top wall, Eq. (33) is used as the boundary condition,

$$\boldsymbol{v_1} = -\omega u_0\left\{e^{-\mathrm{i}[k_\mathrm{s}(W/2+y)-\Delta\varphi]} - e^{-\mathrm{i}[k_\mathrm{s}(W/2-y)+\Delta\varphi]}\right\}\boldsymbol{n} \tag{34}$$

which is the same as Eq. (32) except a phase difference, $\Delta\varphi$. For the water-PZT interface, we assumed that PZT vibrated only in the z direction. Thus, the displacement and the velocity of the substrate at this interface are,

$$\hat{\boldsymbol{u}} = Re(u_\mathrm{T} e^{\mathrm{i}\omega t})\boldsymbol{n} \tag{35}$$

$$\hat{\boldsymbol{v}} = Re(\mathrm{i}\omega u_\mathrm{T} e^{\mathrm{i}\omega t})\boldsymbol{n} \tag{36}$$

where u_T denotes the maximum amplitude of the PZT surface displacement, which is controlled by the applied RF voltage. Again, the continuity of the velocity at the water-PZT interface requires,

$$\boldsymbol{v_1} = \mathrm{i}\omega u_\mathrm{T}\boldsymbol{n} \tag{37}$$

To solve Eqs. (19) and (20) for determining the second order pressure and velocity fields, we assumed the boundary conditions to be $\langle\hat{\boldsymbol{v}}_\mathbf{2}\rangle = 0$ on the channel wall in all model configurations. The boundary condition for $\langle\hat{p}_2\rangle$ was not specified. Instead, we required the average of $\langle\hat{p}_2\rangle$ over the cross-sectional area of the microchannel to be zero.

D. Numerical simulations

Computational mesh with the maximum element dimension d_{b} at the domain boundary and $10d_b$ in the bulk fluid domain is reasonable to capture the physics of the model. We use an illustrative mesh with d_{b}= 30δ, where δ is the viscous penetration depth defined in Eq. (27). For verifying the convergence of the numerical solutions, we defined a relative convergence function $C(\mathrm{g})$,

$$C(\mathrm{g}) = \sqrt{\frac{\int (\mathrm{g}-\mathrm{g}_{\mathrm{ref}})^2 \mathrm{d}y\mathrm{d}z}{\int (\mathrm{g}_{\mathrm{ref}})^2 \mathrm{d}y\mathrm{d}z}} \tag{38}$$

where g is the solution of p_1, v_1 and $<v_2>$ with a given d_{b}, and $\mathrm{g}_{\mathrm{ref}}$ is the reference solution with the smallest d_{b} that was chosen to be 0.2δ in the study. At this dimension, the number of elements was 5.6×10^5 in the simulation domain. We observed that the value of $C(\mathrm{g})$ was less than 0.002 when d_{b} was less than 0.3δ. Therefore, all simulations were performed at this mesh size.

To simulate the fluid flow and particle distribution patterns, we first solved Eqs. (17) and (18) to determine p_1 and $\boldsymbol{v}_1$. The results were substituted into Eqs. (19) and (20) to solve for $\langle\hat{\boldsymbol{v}}_2\rangle$ and $\langle\hat{p}_2\rangle$. Finally, the particle velocity and trajectories were determined by solving Eq. (29).

3. Results and Discussions

A. Acoustofluidic field and particle trajectories in SAW-PDMS and SAW-Glass channels

All simulations were performed with the SAW frequency of 6.65 MHz or the angular frequency of 4.176×10^7 rad/sec. **Fig. 3(a)** shows $Re(p_1)$, the first-order pressure at $t = 2\pi k/\omega$, where k is the wave number. The pressure distribution in the SAW-Glass channel is similar to that reported by Wu's work [32], where the pressure anti-nodes (blue and red) located near the four corners of the channel. Comparing with the pressure distribution in the SAW-PDMS channel, the larger acoustic pressure range in the SAW-Glass channel (Fig. 3(a), right) attributes to the reflected acoustic energy at the water-glass interface.

Fig. 3(b) shows $Re(\boldsymbol{v}_1)$, the first-order velocity at t = 2πk/ω in the SAW-PDMS and SAW-Glass configurations, the amplitude of the actuation velocity (4.2 mm/sec) is less than the amplitude of the first-order velocity $|Re(\boldsymbol{v}_1)|$ in both the SAW-PDMS (5.5 mm/s) and SAW-Glass (38.0 mm/s) structures. The glass reflector reflects 89% of the acoustic energy at the water-glass interface allowing the acoustic wave to travel back to the channel, which results in approximately 7-fold increase in the first-order velocity comparing to that in the SAW-PDMS configuration. The time-averaged streaming velocities, $\langle \hat{\boldsymbol{v}}_2 \rangle$, in the SAW-PDMS and SAW-Glass are shown in **Fig. 3(c)**, with the maximum values of 0.65 μm/s and 5.93 μm/s, respectively.

The velocity and the trajectory of polystyrene microspheres with diameters of 1 μm, 5 μm, and 10 μm were simulated for both the SAW-PDMS and the SAW-Glass configurations, and the results for a period of 10 s are shown in **Fig. 4**. Both channel structures produce streaming rolls when the particle size is 1 μm (**Fig. 4(a)**), the particle velocity in the SAW-Glass channel is much higher than that in the SAW-PDMS. In **Fig. 4(b)**, 5-μm particles are mainly driven by the acoustic radiation force in the SAW-Glass resulting a faster transition to the pressure nodes, while the SAW-PDMS still shows strong streaming effects on the particles. This difference in streaming effect illustrates that the SAW-Glass configuration has a smaller particle transition size at the same frequency than the conventional SAW-PDMS configuration. **Fig. 4(c)** indicates a much higher velocity of 41.0 μm/s achieved in the SAW-Glass for 10-μm particles. The particle velocity in the SAW-Glass is generally larger with the trajectory towards the middle of the channel on the z direction.

B. Acoustofluidic field and particle trajectories in SAW-SAW channel

In the SAW-Glass channel, the reflected wave from the water-glass interface interacts with the wave in the water generated by the bottom SAW transducer to produce the PSW on the z direction. The PSW can be further controlled by using another SAW to replace the glass positioned on the top of the microchannel (see **Fig. 1(c)**). In the SAW-SAW configuration, the phase difference, $\Delta\varphi$, between the two SSAWs generated by the top and the bottom SAW devices can be controlled to manipulate the acoustic energy and pressure distributions within the microchannel. The first-order acoustic pressure

$Re(p_1)$, the first-order velocity field $Re(\boldsymbol{v_1})$, and the time-averaged streaming velocity $\langle \boldsymbol{\hat{v}_2} \rangle$ are shown in **Fig. 5**, where the left and right panels show the results for $\Delta\varphi = 0$ and $\Delta\varphi = \pi$, respectively.

Varying the phase difference $\Delta\varphi$ between the top and bottom SAW transducers can redistribute the pressure gradients and alter the pressure amplitude in the channel, due to the phase shift-induced changes in the positions of the nodes and the anti-nodes [29]. The dependence of the maximum acoustic pressure on $\Delta\varphi$ was obtained by sweeping the $\Delta\varphi$. The results are shown in **Fig. 6(a)**, where shows the largest pressure of 232 kPa. It occurred at $\Delta\varphi = 5\pi/6$ or $7\pi/6$ with four pressure anti-nodes (**Fig. 6(b)**). The smallest pressure is 14 kPa occurring at $\Delta\varphi = 0$ or 2π (**Fig. 5(a)**). The four pressure anti-nodes presented at $\Delta\varphi=5\pi/6$ or $7\pi/6$ are not entirely symmetrical. The acoustic pressure of 224 kPa at $\Delta\varphi = \pi$, which is slightly lower than the maximum ($\Delta\varphi = 5\pi/6$ or $7\pi/6$), is able to produce four symmetrical pressure anti-nodes (**Fig. 5(a)**).

C. Acoustofluidic field and particle trajectories in PZT-SAW channel

The configuration of the hybrid device is shown in **Fig. 1(d)**. Compared with the SAW-SAW configuration, the acoustic pressure in the PZT-SAW channel is higher than that with $\Delta\varphi = 0$, but less than the pressure with $\Delta\varphi = \pi$ (see **Fig. 5** and **Fig. 7(a)**). To allow high throughput particle manipulation by the primary acoustic radiation force to drive particles towards a belt-like distribution in the z direction[32], it is desired to have two pressure anti-nodes aligned vertically in the channel. We found that it could be achieved by increasing the vibration amplitude of the PZT transducer, e.g., $u_T = 10u_0$. In this case, two pressure anti-nodes were formed (see **Fig. 7(b)**), and the acoustic pressure is higher than that in the SAW-SAW configuration, allowing more power for particle manipulation.

To investigate other acoustic pressure values at various microchannel dimensions in the PZT-SAW configuration, we swept the microchannel width (W) and height (H) from $\lambda/2$ to λ, and from $\lambda/8$ to $\lambda/4$, respectively. The maximum acoustic pressure for each set of W and H is shown in **Fig. 8(a)** for $u_T = u_0$ and **Fig. 8(b)** for $u_T = 10u_0$. The largest acoustic pressure of 434 kPa is noted with pressure anti-nodes reduced to two for $u_T = u_0$, and 4,080 kPa for $u_T = 10u_0$. These results demonstrate that changing the dimension of the microchannel is more effective than increasing u_T (see **Fig. 7b**) for driving the particles towards a belt-like distribution. The results show potential applications for rapid alignment of particles in the microchannel.

Fig. 9 shows the particle trajectories in the SAW-SAW configuration for $\Delta\varphi = \pi$ and the PZT-SAW configuration for $u_T = 10u_0$. Particles with 1 μm diameter in the SAW-SAW microchannel form 4 streaming rolls with a vague sign being distributed on the vertical belt region, while a better tendency of distribution present in the PZT-SAW (Fig. 9a). Since 1 μm is smaller than the transition size, these particles are mainly experiencing drag force. For the sizes of 5 μm and 10 μm, effective trapping is noted in both the SAW-SAW and the PZT-SAW configurations (Figs. 9b & 9c). The latter one achieves the maximum particle velocity of 76 mm/s and 270 mm/s for 5 μm and 10 μm particles, respectively, with the final distribution fully located at the vertical belt region.

D. Manipulation effectiveness and efficiency

The effectiveness and efficiency of the four different configurations for particle manipulation are shown in Figs. 10a to 10d. In generally, both the PZT-SAW and SAW-SAW devices demonstrate quicker migration for three sizes of particles comparing to the SAW-PDMS and SAW-Glass structures. For example, more than 88% of the 5-μm and 10-μm particles arrive the pressure node area within 10 sec in the PZT-SAW while only up to 30% of them meet the pressure node area in the SAW-PDMS. The slope of the percentage also indicates that the SAW-SAW configuration works more efficiently comparing with the SAW-GLASS; the latter takes longer time to migrate particles to the pressure node area. Fig. 10e shows the percentage of particles aggregated after 20 sec. Both the PZT-SAW and the SAW-SAW configurations show a better manipulation efficiency for most of the particle sizes. 84.8% and 89.3% 5-μm particles and 87.5% and 91.5% 10-μm particles are observed in the target area respectively. For 1-μm particles, these hybrid structures also demonstrate better aggregation as they migrate 73.0% and 58.4%, respectively, which are considerably higher than both the SAW-Glass and SAW-PDMS configurations.

4. Conclusions

A comprehensive comparison amongst traditional SAW-PDMS, hybrid SAW-Glass, SAW-SAW, and PZT-SAW structures have been presented in the study. The model of the SAW-SAW configuration notably increased the 10-μm particle velocity to 582 μm/s, comparing to the velocity of 41 μm/s in the state-of-the-art hybrid SAW-Glass configuration. This improvement is achieved by introducing the top SAW transducer instead of the passive reflection/absorber used in most of acoustofluidic devices. Furthermore, the study shows that the longitudinal wave produced by the top PZT actuator in the PZT-SAW model can interact with the acoustic wave generated by the bottom SAW transducer to enable a stronger acoustic resonance in the microchannel. The enhanced acoustic pressure exerts higher acoustic radiation force on particles resulting in faster particle motion and higher manipulation throughput. The future work is to manufacture the SAW-SAW and PZT-SAW acoustofluidic chips to experimentally verify the predications from the numerical analysis.

Acknowledgement

This work was funded by the Engineering and Physical Sciences Research Council UK (EP/P002803/1) , the Royal Society International Exchanges 2017 Cost Share (IEC\NSFC\170142) and Natural Science Foundation of China (NSFC) (61704017).

Reference

1. S. Li, F. Ma, H. Bachman, C. E. Cameron, X. Zeng and T. J. Huang, *Journal of micromechanics and microengineering : structures, devices, and systems*, 2017, **27**.
2. Y. Ai, C. K. Sanders and B. L. Marrone, *Analytical chemistry*, 2013, **85**, 9126-9134.
3. S. Toru, M. Frenea-Robin, N. Haddour and F. Buret, *Conference proceedings: Annual International Conference of the IEEE Engineering in Medicine and Biology Society. IEEE Engineering in Medicine and Biology Society. Annual Conference*, 2012, **2012**, 4998-5001.
4. G. P. Gautam, T. Burger, A. Wilcox, M. J. Cumbo, S. W. Graves and M. E. Piyasena, *Analytical and bioanalytical chemistry*, 2018, **410**, 3385-3394.

5. F. Petersson, L. Aberg, A. M. Sward-Nilsson and T. Laurell, *Analytical chemistry*, 2007, **79**, 5117-5123.
6. J. Nam, H. Lim, D. Kim and S. Shin, *Lab on a chip*, 2011, **11**, 3361-3364.
7. Y. Chen, M. Wu, L. Ren, J. Liu, P. H. Whitley, L. Wang and T. J. Huang, *Lab on a chip*, 2016, **16**, 3466-3472.
8. Z. Ma, Y. Zhou, D. J. Collins and Y. Ai, *Lab on a chip*, 2017, **17**, 3176-3185.
9. J. Lei, P. Glynne-Jones, M. J. M. Hill and Nanofluidics, 2017, **21**, 23.
10. M. Antfolk, C. Antfolk, H. Lilja, T. Laurell and P. Augustsson, *Lab on a chip*, 2015, **15**, 2102-2109.
11. P. Li, Z. Mao, Z. Peng, L. Zhou, Y. Chen, P. H. Huang, C. I. Truica, J. J. Drabick, W. S. El-Deiry, M. Dao, S. Suresh and T. J. Huang, *Proceedings of the National Academy of Sciences of the United States of America*, 2015, **112**, 4970-4975.
12. M. Antfolk, C. Magnusson, P. Augustsson, H. Lilja and T. Laurell, *Analytical chemistry*, 2015, **87**, 9322-9328.
13. A. Ku, H. C. Lim, M. Evander, H. Lilja, T. Laurell, S. Scheding and Y. Ceder, *Analytical chemistry*, 2018, **90**, 8011-8019.
14. K. Lee, H. Shao, R. Weissleder and H. Lee, *ACS nano*, 2015, **9**, 2321-2327.
15. M. Wu, Y. Ouyang, Z. Wang, R. Zhang, P. H. Huang, C. Chen, H. Li, P. Li, D. Quinn, M. Dao, S. Suresh, Y. Sadovsky and T. J. Huang, *Proceedings of the National Academy of Sciences of the United States of America*, 2017, **114**, 10584-10589.
16. X. Ding, P. Li, S. C. Lin, Z. S. Stratton, N. Nama, F. Guo, D. Slotcavage, X. Mao, J. Shi, F. Costanzo and T. J. Huang, *Lab on a chip*, 2013, **13**, 3626-3649.
17. L. Ren, Y. Chen, P. Li, Z. Mao, P. H. Huang, J. Rufo, F. Guo, L. Wang, J. P. McCoy, S. J. Levine and T. J. Huang, *Lab on a chip*, 2015, **15**, 3870-3879.
18. H. Guo, Y. Zheng, B. Wang and Z. Li, *Sensors (Basel, Switzerland)*, 2015, **15**, 25033-25038.
19. R. Barnkob, P. Augustsson, T. Laurell and H. Bruus, *Physical review. E, Statistical, nonlinear, and soft matter physics*, 2012, **86**, 056307.
20. P. B. Muller, R. Barnkob, M. J. Jensen and H. Bruus, *Lab on a chip*, 2012, **12**, 4617-4627.
21. S. P. Zhang, J. Lata, C. Chen, J. Mai, F. Guo, Z. Tian, L. Ren, Z. Mao, P. H. Huang, P. Li, S. Yang and T. J. Huang, *Nature communications*, 2018, **9**, 2928.
22. Y. Bourquin, J. Reboud, R. Wilson and J. M. Cooper, *Lab on a chip*, 2010, **10**, 1898-1901.
23. C. Chen, S. P. Zhang, Z. Mao, N. Nama, Y. Gu, P.-H. Huang, Y. Jing, X. Guo, F. Costanzo and T. J. Huang, *Lab on a chip*, 2018, **18**, 3645-3654.
24. F. Wu, M. H. Shen, J. Yang, H. Wang, R. Mikhaylov, A. Clayton, X. Qin, C. Sun, Z. Xie and M. Cai, *IEEE Electron Device Lett*, 2021, **42**, 577-580.
25. R. Mikhaylov, F. Wu, H. Wang, A. Clayton, C. Sun, Z. Xie, D. Liang, Y. Dong, F. Yuan and D. Moschou, *Lab Chip*, 2020, **20**, 1807-1814.
26. R. Barnkob, P. Augustsson, T. Laurell and H. Bruus, *Physical Review E*, 2012, **86**, 056307.
27. N. R. Skov and H. Bruus, 2016, **7**, 182.
28. J. Guo, Y. Kang and Y. Ai, *Journal of Colloid and Interface Science*, 2015, **455**, 203-211.
29. N. Nama, R. Barnkob, Z. Mao, C. J. Kahler, F. Costanzo and T. J. Huang, *Lab on a chip*, 2015, **15**, 2700-2709.
30. C. Sun, F. Wu, Y. Fu, D. J. Wallis, R. Mikhaylov, F. Yuan, D. Liang, Z. Xie, H. Wang and R. Tao, *Ultrasonics*, 2020, **108**, 106202.
31. R. Barnkob, N. Nama, L. Ren, T. J. Huang, F. Costanzo and C. J. Kähler, *Physical Review Applied*, 2018, **9**, 014027.
32. M. Wu, P. H. Huang, R. Zhang, Z. Mao, C. Chen, G. Kemeny, P. Li, A. V. Lee, R. Gyanchandani, A. J. Armstrong, M. Dao, S. Suresh and T. J. Huang, *Small (Weinheim an der Bergstrasse, Germany)*, 2018, **14**, e1801131.

33. M. Wu, K. Chen, S. Yang, Z. Wang, P. H. Huang, J. Mai, Z. Y. Li and T. J. Huang, *Lab on a chip*, 2018, **18**, 3003-3010.
34. H. Bruus, *Lab on a chip*, 2012, **12**, 20-28.
35. J. S. Bach and H. Bruus, 2018, **144**, 766-784.
36. M. Settnes and H. Bruus, *Physical Review E*, 2012, **85**, 016327.
37. H. Bruus, *Lab on a chip*, 2012, **12**, 1014-1021.
38. Z. Mao, Y. Xie, F. Guo, L. Ren, P. H. Huang, Y. Chen, J. Rufo, F. Costanzo and T. J. Huang, *Lab on a chip*, 2016, **16**, 515-524.

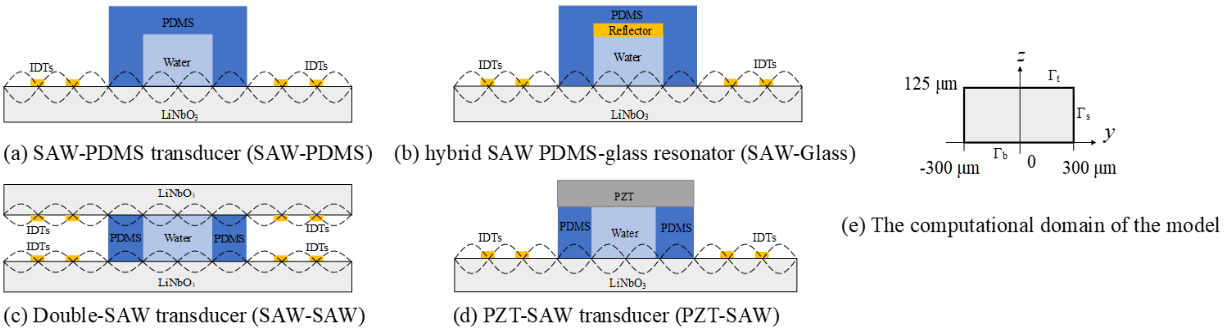

Figure 1. (a) A typical acoustofluidic structure consisting of a PDMS microchannel and a SAW transducer (SAW-PDMS). (b) A hybrid acoustofluidic resonator employing a glass slide as the reflector positioned at the top of the PDMS microchannel (SAW-Glass). (c) A novel acoustofluidic configuration equipped by two SAW transducers as the top and bottom plates (SAW-SAW). (d) An integrated acoustofluidic configuration consisting of a top PZT and a bottom SAW transducer (PZT-SAW). (e) The computational domain of the model, the boundary Γ_t, Γ_b, and Γ_s are modelled as the top, bottom and side walls, respectively, with the choice of different boundary conditions in the SAW-PDMS, SAW-Glass, SAW-SAW, and PZT-SAW models.

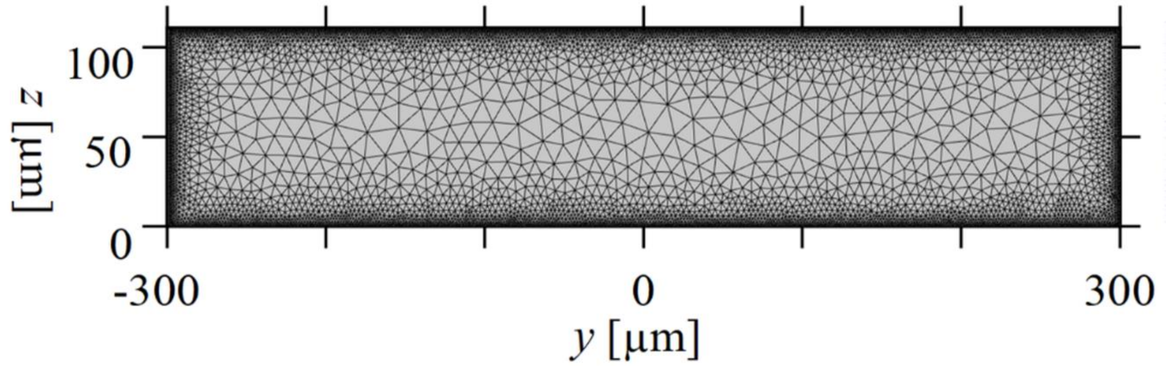

Figure 2 The mesh obtained with a maximum element size $d_{\mathrm{mesh}} = 30\delta$, constituting 2478 triangular elements.

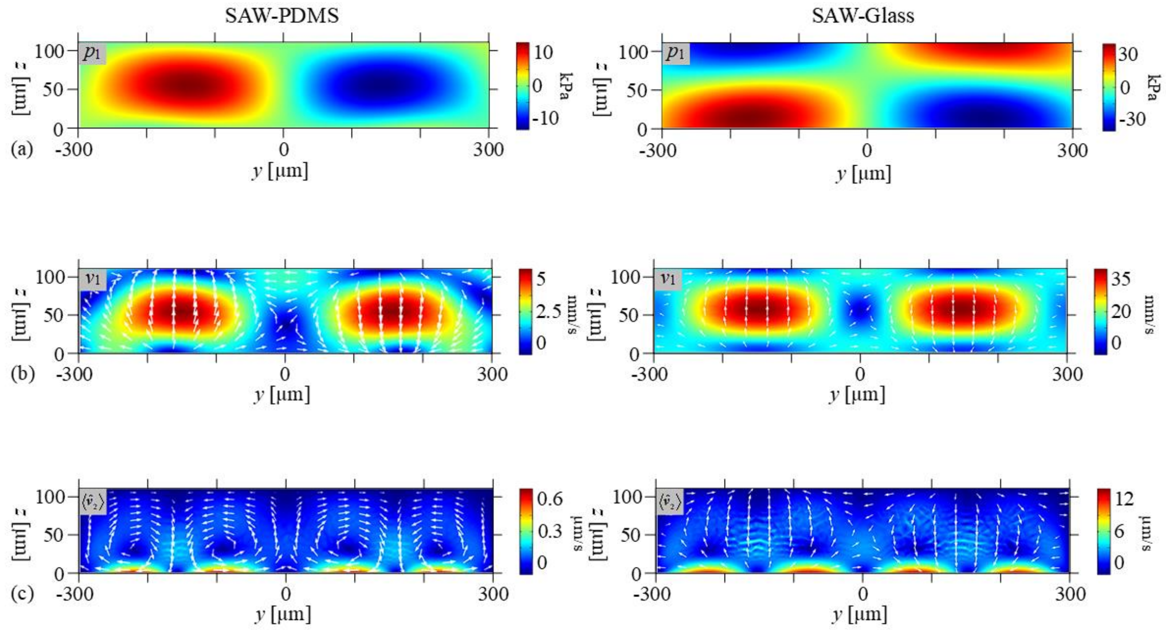

Figure 3 Colour plots of the first-order acoustic pressure p_1, the first-order velocity field $\boldsymbol{v}_1$ and the time-averaged second-order velocity $\langle \hat{\boldsymbol{v}}_2 \rangle$ in the SAW-PDMS and SAW-Glass channels. (a) The maximum pressure in the SAW-PDMS and SAW-Glass is 13.3 kPa and 33.6 kPa, respectively. (b) The amplitude of the first-order velocity in the SAW-PDMS and SAW-Glass is 5.5 mm/s and 38.0 mm/s, respectively. (c) The maximum second-order velocity in the SAW-PDMS and SAW-Glass is 0.65 μm/s and 5.93 μm/s, respectively.

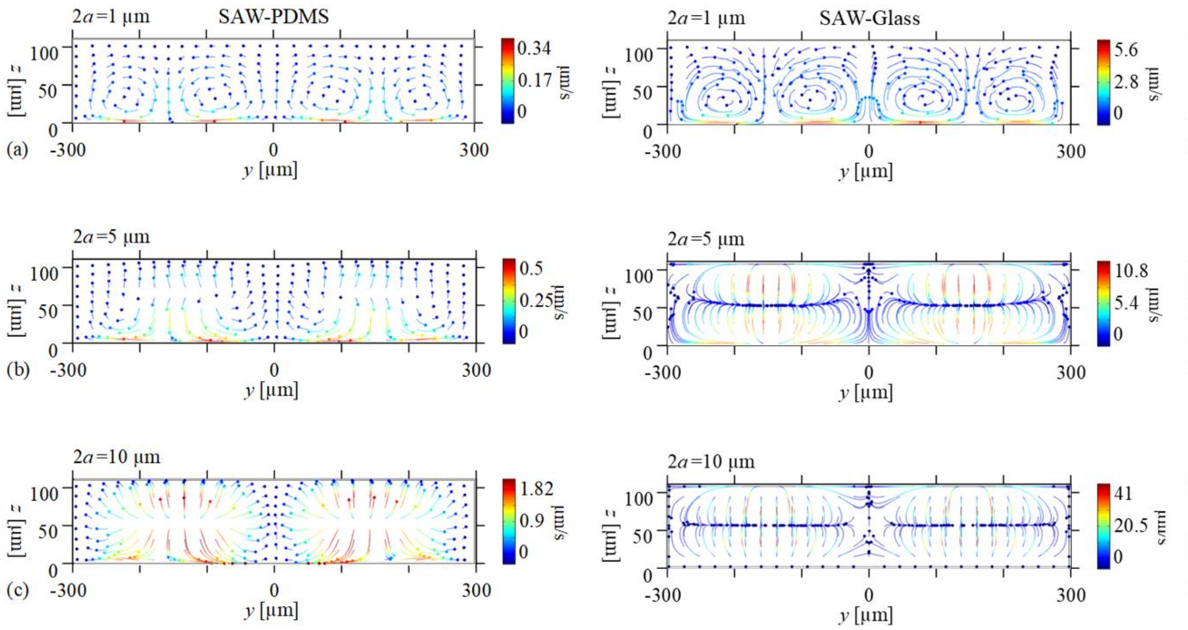

Figure 4 Particle trajectories and velocities in the SAW-PDMS and SAW-Glass configurations. (a) Particle size is 1 µm, the maximum velocity is 0.34 µm/s in SAW-PDMS and 5.6 µm/s in SAW-Glass. (b) Particle size is 5 µm, the maximum velocity is 0.5 µm/s in SAW-PDMS and 10.8 µm/s in SAW-Glass. (c) Particle size is 10 µm, the maximum velocity is 1.82 µm/s in SAW-PDMS and 41 µm/s in SAW-Glass.

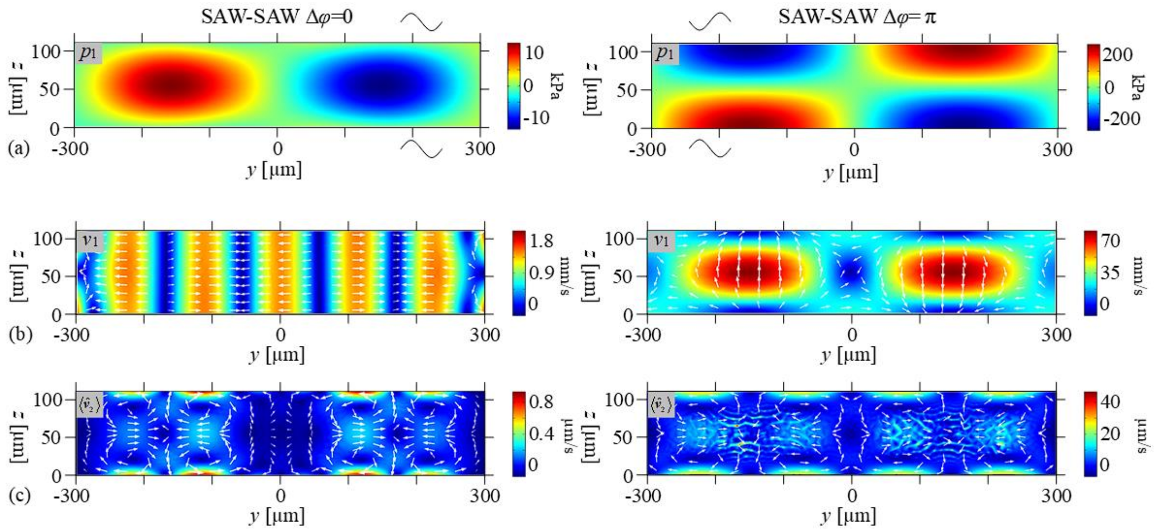

Figure 5 Colour plots of the first-order acoustic pressure p_1, the first-order velocity field $\boldsymbol{v_1}$ and the time-averaged second-order velocity $\langle \boldsymbol{\hat{v}_2} \rangle$ in the SAW-SAW channel. The left panel shows the phase difference $\Delta\varphi = 0$ while the right panel shows the phase different $\Delta\varphi = \pi$. (a) The maximum pressure is 14 kPa and 224 kPa, respectively. (b) The amplitude of the first-order velocity is 1.8 mm/s and 70.0 mm/s, respectively. (c) The maximum second-order velocity is 0.8 μm/s and 31.0 μm/s, respectively.

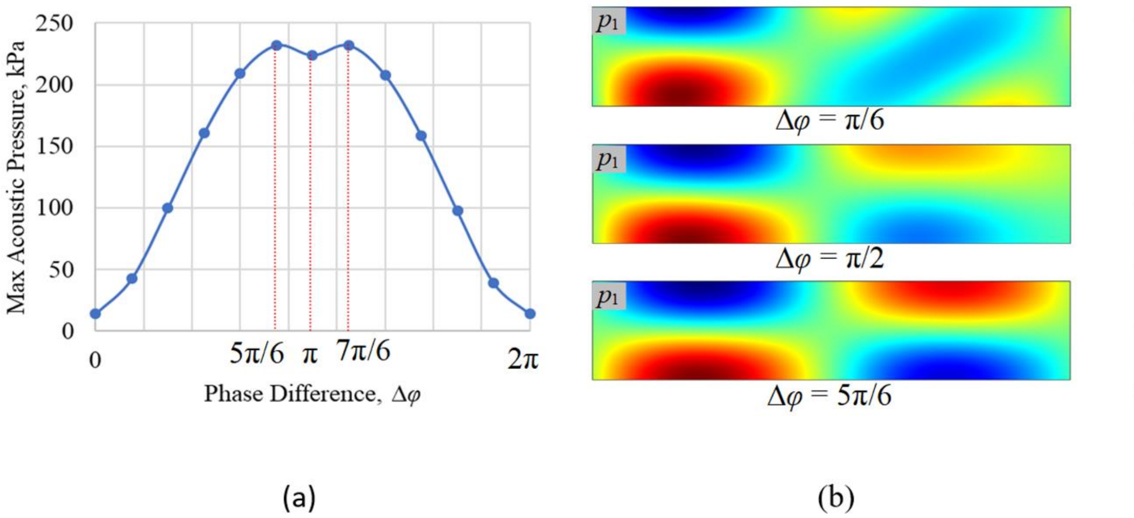

Figure 6 Plots of the maximum first-order acoustic pressure p_1 (a) and the acoustic pressure distribution (b) for phase difference $\Delta\varphi$ between 0 and 2π in the SAW-SAW configuration.

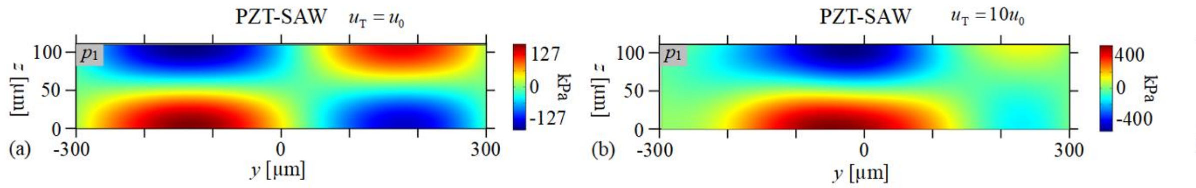

Figure 7 Colour plots of the first-order acoustic pressure p_1 for the PZT-SAW configuration when the amplitude of the vibration of the PZT is (a) the same as the SAW transducer, and (b) 10 times higher than the SAW transducer.

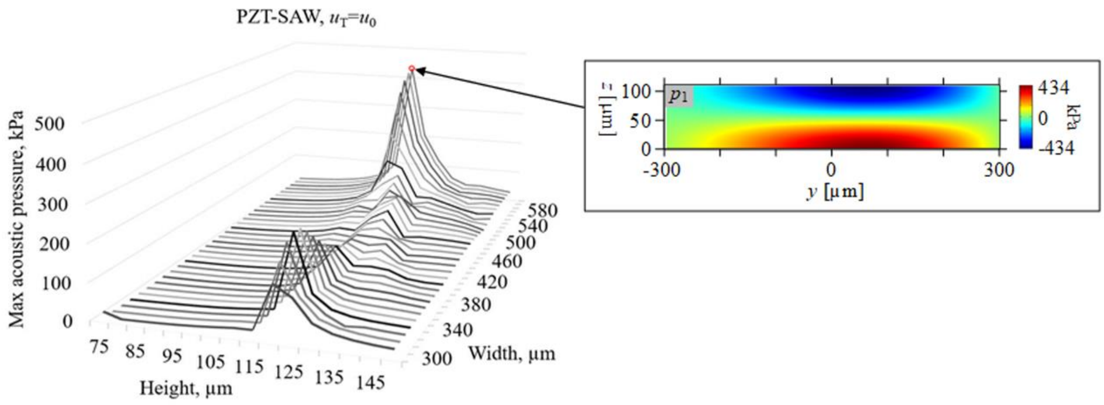

(a)

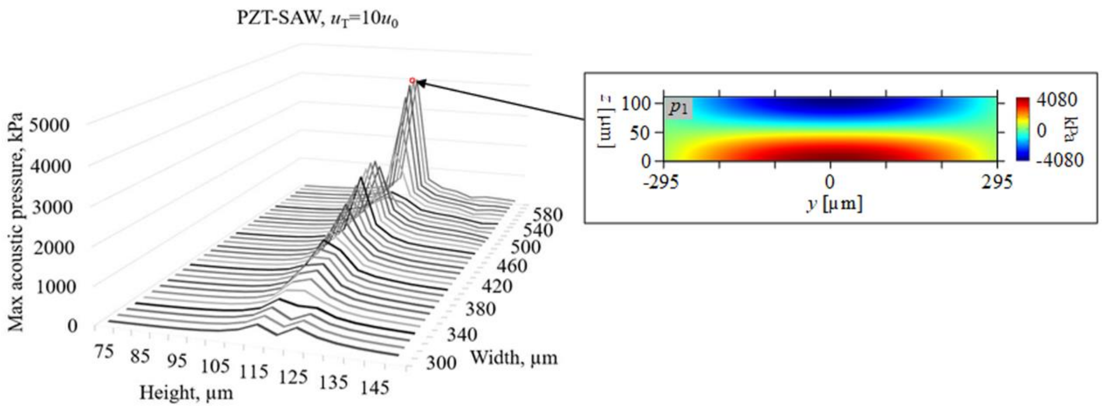

Figure 8. 3D lines of the maximum acoustic pressures for dimension sweep for (a) $u_{\mathrm{T}} = u_0$, (b) $u_{\mathrm{T}} = 10u_0$. Maximum acoustic pressures were noted at 600 µm (W) × 115 µm (H) and 590 µm (W) × 115 µm (H) for $u_{\mathrm{T}} = u_0$ and $u_{\mathrm{T}} = 10u_0$, respectively. Insets correspond the first-order acoustic pressures.

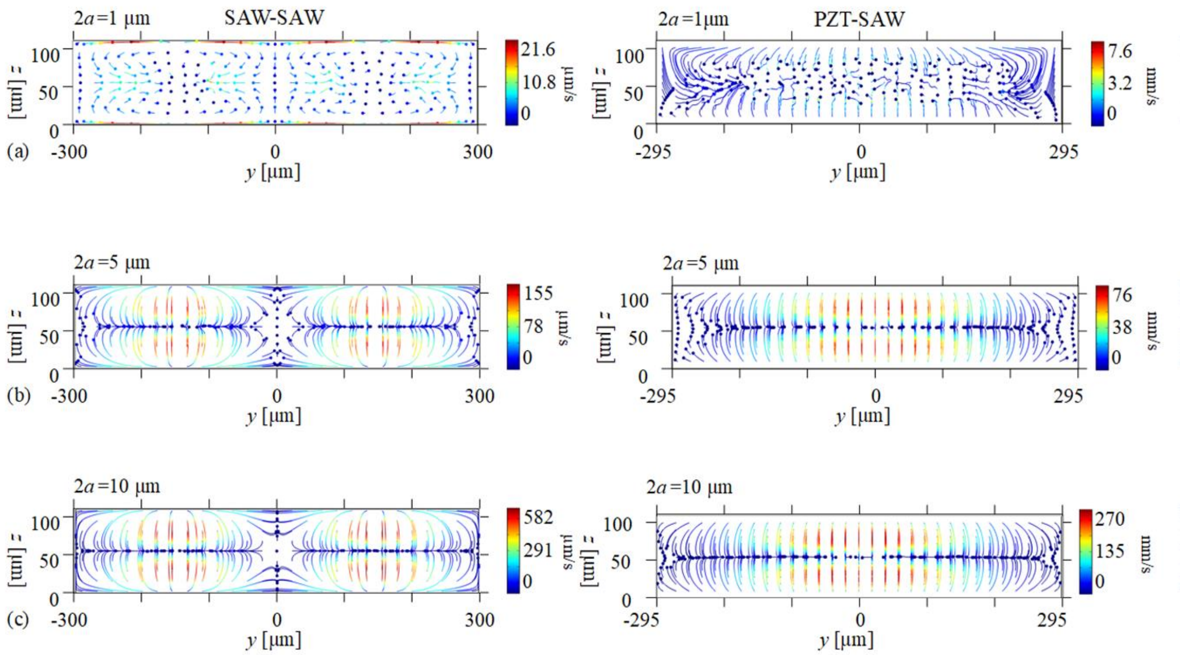

Figure 9 Particle trajectories and velocities in the SAW-SAW (phase difference $\Delta\varphi = \pi$) and PZT-SAW ($u_{\mathrm{T}} = 10u_0$) configurations. (a) Particle size is 1 μm, the maximum velocity is 21.6 μm/s in SAW-SAW and 7.6 mm/s in PZT-SAW. (b) Particle size is 5 μm, the maximum velocity is 155 μm/s in SAW-SAW and 76 mm/s in PZT-SAW. (c) Particle size is 10 μm, the maximum velocity is 582 μm/s in SAW-SAW and 270 mm/s in PZT-SAW.

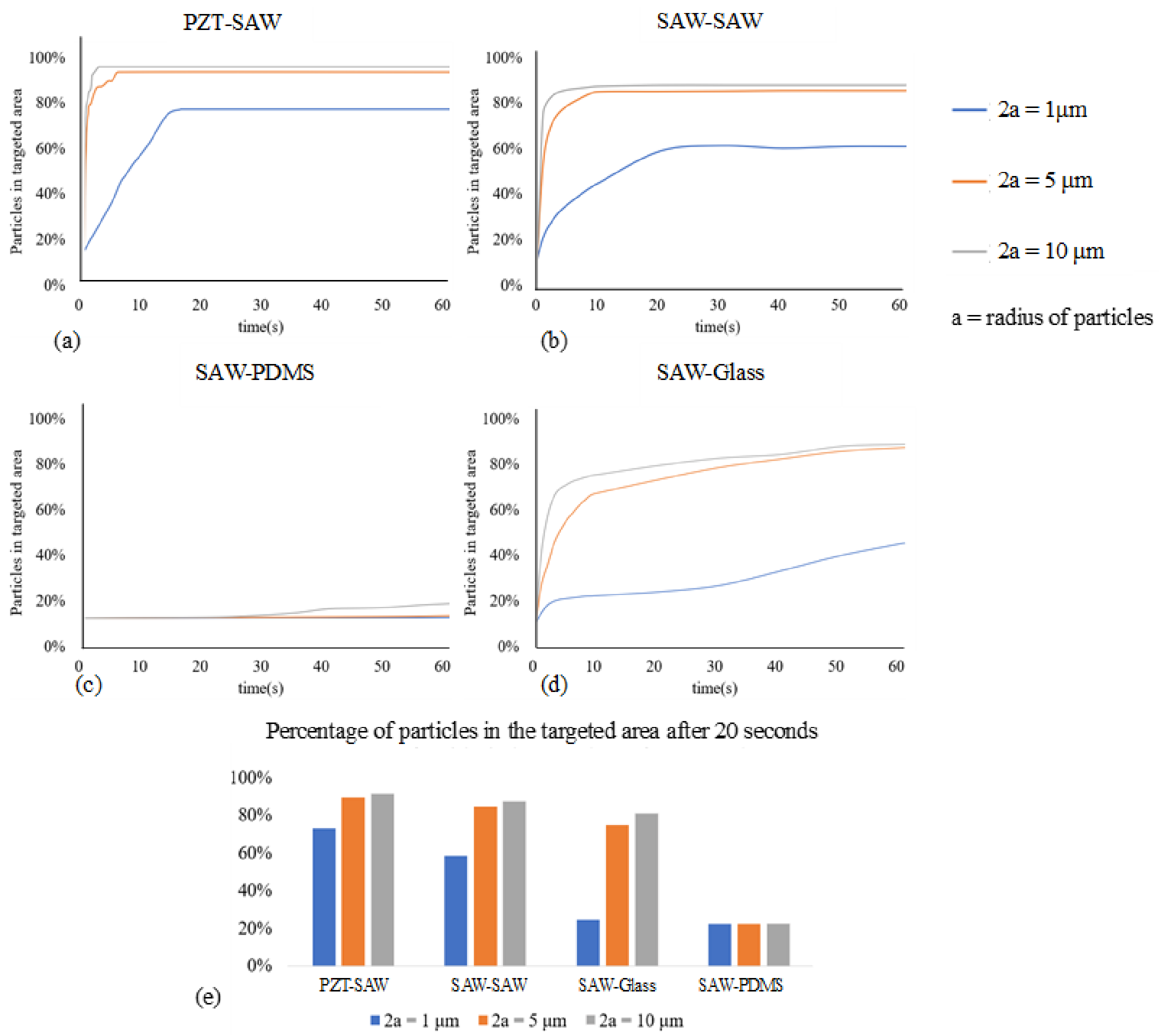

Figure 10 Manipulation effectiveness and efficiency of four different configurations.

Table 1 The parameters used in simulations

Water		
Density	ρ_0	997 kg/m^3
Speed of sound	c_0	1497 m/s
Shear viscosity	η	0.890 mPa s
Bulk viscosity	η_b	2.47 mPa s
Compressibility[a]	κ_0	448 TPa^{-1}
Polystyrene		
Density	ρ_p	1050 kg/m^3
Compressibility[b]	κ_p	249 Tpa^{-1}
Acoustic actuation parameters		
Wavelength	λ	600 μm
Forcing frequency	f	6.65 MHz
Displacement amplitude	u_0	0.1 nm
Acoustic impedance		
PDSM	Z_{PDMS}	0.99 MPa·s/m
Glass	Z_{glass}	12.0 MPa·s/m